

Low-sintering-temperature garnet oxides by conformal sintering-aid coating

Shaojie Chen

ShanghaiTech University

Xiangchen Hu

ShanghaiTech University

Wenda Bao

ShanghaiTech University

Zeyu Wang

ShanghaiTech University

Qun Yang

University of Illinois at Urbana Champaign

Lu Nie

ShanghaiTech University

Xun Zhang

ShanghaiTech University

Jingxuan Zhang

ShanghaiTech University

Yilan Jiang

ShanghaiTech University <https://orcid.org/0000-0001-8388-8946>

Yi Han

State Key Lab of New Ceramics and Fine Processing, School of Materials Science and Engineering, Tsinghua University, Beijing, P. R. China, 100084

Chunlei Wan

State Key Lab of New Ceramics and Fine Processing, School of Materials Science and Engineering, Tsinghua University, Beijing, P. R. China, 100084

Jin Xie

ShanghaiTech University <https://orcid.org/0000-0002-6270-1465>

Yi Yu

ShanghaiTech University <https://orcid.org/0000-0003-4326-5992>

Wei Liu (✉ liuwei1@shanghaitech.edu.cn)

ShanghaiTech University <https://orcid.org/0000-0002-6206-8321>

Keywords: Garnet-type Solid Electrodes, Conformal Coating, Nanoscale Amorphous Alumina, Ionic Conductivity

Posted Date: March 10th, 2021

DOI: <https://doi.org/10.21203/rs.3.rs-243848/v1>

License:  This work is licensed under a Creative Commons Attribution 4.0 International License.

[Read Full License](#)

Abstract

Garnet-type solid electrolytes have attracted an extensive attention for high-energy solid-state lithium batteries. However, the high processing temperature up to 1200°C with high cost limits the large-scale production. Here, we report a simple approach to reduce the sintering temperature by a conformal coating of nanoscale amorphous alumina, without sacrificing ionic conductivity. The ceramic sintered at 980°C shows a high ionic conductivity of 0.13 mS cm^{-1} at room temperature. It reveals that the second phase segregated at grain boundaries can promote Li-ion transport, block electronic conduction, and improve mechanical property. The Li symmetry cells using this garnet electrolyte indicate a long-term 2500 cycle life and a high critical current density of 0.52 mA cm^{-2} . The garnet electrolyte enables the high-voltage cells using $\text{Li}_{1.2}\text{Ni}_{0.2}\text{Mn}_{0.6}\text{O}_2$ to deliver a high specific capacity of 248 mAh g^{-1} at 0.05 C-rate. This work provides a new clue to lower sintering temperature for garnet electrolytes, which can extend to other ceramics towards practical applications.

Introduction

Lithium-ion batteries (LIBs) as energy storage devices are widely used in commercial electronics and electric vehicles. Potential safety risk and limited energy density have become two bottle-neck problems for commercial LIBs utilizing organic liquid electrolyte¹⁻³. Under such circumstance, solid-state lithium-metal batteries (SSLMBs) using solid electrolytes (SEs) and Li metal anode, is the most promising direction to address above issues⁴⁻⁸. Garnet-type oxide electrolyte $\text{Li}_7\text{La}_3\text{Zr}_2\text{O}_{12}$ (LLZO) has attracted increasing attention owing to its high room-temperature (RT) ionic conductivity (10^{-4} - $10^{-3} \text{ S cm}^{-1}$), wide electrochemical potential window, and high chemical stability against Li metal⁹⁻¹¹. Moreover, the LLZO ceramic exhibits high Young's modulus ($\sim 150 \text{ GPa}$) and shear modulus ($\sim 60 \text{ GPa}$)^{12,13}, which is expected to suppress Li dendrite growth according to Newman and Monroe's prediction¹⁴. However, experiments revealed that Li dendrites could penetrate LLZO along the grain boundaries and voids¹⁵⁻¹⁹. More recent works demonstrated that the high electronic conductivity (10^{-8} - $10^{-7} \text{ S cm}^{-1}$ at RT) inside LLZO and on the surface could facilitate the Li dendrite propagation inside LLZO²⁰⁻²². Consequently, the critical current density (CCD), at which the cell is shorted by Li dendrite growth, is always less than 1.0 mA cm^{-2} at RT, which is at some distance from the practical requirement^{13,15,21,23}. Therefore, approaches on strengthening grain boundary and reducing electronic conductivity of garnet SEs are highly desired.

Additionally and importantly, the garnet ceramic fabrication generally requires a high sintering temperature above 1100 °C for the purpose of densification and obtaining high ionic conductivity of above 0.1 mS cm^{-1} ²⁴. Reducing sintering temperature with reduced holding time is an energy saving, cost effective and large-scaled development direction for preparing garnet electrolytes, which can further facilitate co-sintering SE with electrode materials (for example, LiCoO_2 ²⁵ and $\text{LiNi}_{0.5}\text{Co}_{0.2}\text{Mn}_{0.3}\text{O}_2$ ²⁶). Existed approaches on reducing sintering temperature include thin-film fabrication²⁴, hot press sintering^{27,28}, spark plasma sintering (SPS)²⁹, microwave-assisted sintering³⁰ and so on. While, these

fabrications are high cost and the garnet thin films exhibit three to five orders of magnitude lower ionic conductivity than its bulky counterparts. Comparatively, the traditional method of solid-state reaction with pressureless sintering is the most cost effective, but sintering additive is needed to reduce the sintering temperature. The sintering aids, including alumina³¹⁻³³, Li₃BO₃²⁵ and Li₄SiO₄³⁴, have been widely investigated to lower sintering temperature for garnet electrolytes. However, the sintering aids are usually mixed physically by ball milling in form of crystallized particles or sheets, causing an inhomogeneous distribution, which restricts the sintering temperature over 1100 °C²⁴.

Here, we adopt a conformal nano-coating of amorphous alumina as sintering aid to prepare the garnet solid electrolyte by conventional pressureless sintering. As shown in Fig. 1, compared with the physical mixing, the method of conformal sintering aid coating could access the sintering temperature below 1000 °C for the garnet ceramic, without sacrificing its ionic conductivity. The forming Li-Al-O second phase uniformly distributed at the grain boundaries can effectively enhance sintering activity and subsequently promote the densification. Moreover, the Li-Al-O second phase is ionically conductive but electronically insulative, which can enhance the ionic conductivity of grain boundary while decrease the electronic conductivity. As a result, a higher CCD value and longer cycling life could be successfully achieved.

Phase And Morphology

To improve sintering activity and reduce processing temperature, we introduced nanoscale amorphous alumina coating on the ceramic particle surfaces conformally by atomic layer deposition (ALD) technology, instead of traditional method of physical mixing sintering aids with ceramic powders. We denote Ta-doped LLZO (LLZTO) without sintering additive as LLZTO w/o alumina, the one with alumina powders by ball milling as LLZTO+alumina and the one with alumina nano-coating by ALD as LLZTO@alumina. The X-Ray diffraction (XRD) patterns of pure LLZTO powder and LLZTO@alumina powder (Fig. 2A) indicate that both samples have a cubic garnet crystal structure without impurity forming during the ALD process. Note that the absence of alumina in the XRD pattern is owing to the alumina layer is amorphous.

The LLZTO@alumina core@shell structure is proved through transmission electron microscopy (TEM) observation, as shown in Fig. 2B. The LLZTO particle is conformally covered by an amorphous alumina layer. It can be observed that the thickness of alumina coating is about 2 nm. Notably, compared to different thickness of 1, 5 and 10 nm, 2 nm of alumina coating layer thickness is the optimal value. As shown in Fig. S1, the LLZTO@alumina-2 nm pellet has the highest ionic conductivity. When the thickness is smaller than 2 nm, the amount of sintering aid is not adequate. And when the thickness is larger than 2 nm, the redundant sintering aid results in the excessive accumulation of second phase in the grain boundaries, showing a larger grain-boundary resistance. Figure 2C is the corresponding selected area electron diffraction (SAED) pattern, demonstrating a cubic garnet structure, which is consistent with the XRD results. The energy-dispersive X-ray spectroscopy (EDS) mapping of the LLZTO@alumina particle was displayed in Fig. 2D. The Zr and La elements from LLZTO core and Al element from alumina shell are homogeneously distributed over the entire particle, indicating the LLZTO particle is totally covered by

alumina coating. Moreover, the EDS and corresponding mapping images of pure LLZTO particle are shown in Fig. S2. There is nearly no Al element signal, indicating the Al element in the LLZTO@alumina is introduced in the process of ALD. Figure S3 displays the EDS mapping of a plurality of LLZTO@alumina particles. Al element is also evenly distributed on all the particles, further proving the uniformity of alumina coating. The X-ray photoelectron spectroscopy (XPS) results of the pure LLZTO and LLZTO@alumina powders are shown in Fig. 2E. It can be seen that a peak of Al 2p appears in the spectra of LLZTO@alumina powder, which is absent in that of LLZTO powders. The XPS results are in great agreement with the EDS results.

Next, the structures of the sintered LLZTO pellets were characterized. The XRD patterns of the samples prepared with various sintering conditions were shown in Fig. S4, all showing the cubic phase. In addition, the elemental compositions of LLZTO samples determined by inductively coupled plasma-optical emission spectroscopy (ICP-OES) are listed in Table S1, which is consistent with our expected composition. It is generally recognized that the mother powder having the same composition with the green garnet pellet is often used to compensate the Li-loss during high-temperature sintering process. To further investigate the influence of the alumina nano-coating for Li loss during sintering process, the XRD patterns of different LLZTO pellets without using mother powder are shown in Fig. S5. We can see that the LLZTO@alumina-1000 shows a relatively weaker peak signal of $\text{La}_2\text{Zr}_2\text{O}_7$ than LLZTO-1000 (the number is sintering temperature), given that $\text{La}_2\text{Zr}_2\text{O}_7$ is widely considered to be the impurity product after Li-loss for LLZO³⁵. This result shows that the conformal alumina coating can also suppress the Li-loss during sintering, thus reducing the material cost.

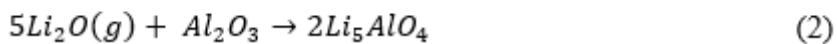
In addition, the morphologies of LLZTO w/o alumina, LLZTO+alumina and LLZTO@alumina sintered pellets have been characterized using scanning electron microscopy (SEM) (Fig. S6 and Fig. 3A-F). The LLZTO w/o alumina sample sintered at 1100 °C has a loose cross-section-view morphology, showing the LLZTO cannot be well-sintered without sintering aid. And with the sintering temperature increases to 1200 °C, abnormal grain growth occurs (Fig. S6C)³¹. As shown in Fig. 3B, the LLZTO+alumina sample sintered at 1000 °C is not well sintered with many pores and uneven grain size distribution (Fig. S7). After enhancing the sintering temperature to 1100 °C, pores disappear and average grain size increases from 2.03 μm to 2.36 μm. While, for the LLZTO@alumina sample sintered at 1000 °C, the cross-section-view SEM shows a very dense microstructure with an average grain size of 2.36 μm. It should be noted that increasing sintering temperature to 1100 °C cannot further promote the densification of the ceramic pellets (Fig. 3F). Besides, as shown in Fig. 3A and D, the LLZTO@alumina pellet sintered at a low temperature of 980 °C shows a relative dense microstructure, while the LLZTO+alumina sintered at 980 °C has a loose microstructure. These results indicate that the approach of conformal coating of sintering aid is much more effective than the traditional physical mixing method.

The EDS maps of LLZTO+alumina and LLZTO@alumina pellet are shown in Fig. 3G and Fig. 3H, respectively. Firstly, the dark contrast in the mapping of O element corresponds to pores in the ceramic electrolyte. We can distinguish that there are a large number of pores for LLZTO+alumina, while few pores for LLZTO@alumina. Secondly, combining the distribution of O and Al elements, we can find out

the O-rich region and Al-rich region are nearly overlapped and located at grain boundaries, which is the Li-Al-O second phases formed along grain boundaries. Auger electron spectroscopy (AES) was used to further distinguish the components of grain and grain boundary (Fig. 3I). The Li, Al and O elements were detected both on the grain and grain boundary area. For LLZTO+alumina sample, the Li/Al ratios of grain and grain boundary are 2.42 and 1.39, respectively. And for LLZTO@alumina sample, the Li/Al ratios of grain and grain boundary are 1.32 and 1.09, indicating that more Al element was doped into grain than LLZTO+alumina sample.

To investigate the microstructure of the second phase, aberration-corrected TEM and scanning transmission electron microscopy (STEM) were applied. Figure 4A shows a TEM image of a second phase region formed at a triangular grain boundary region of LLZTO@alumina pellet. The second phase is surrounded by LLZTO which shows darker contrast. The SAED pattern (Fig. 4B) taken from the second phase is consistent with α -Li₅AlO₄ viewed along zone axis [112]. The aberration-corrected high-resolution TEM (AC-HRTEM) image of triangular grain boundary area is shown in Fig. 4C (left) and the corresponding Fourier transform pattern (inset) agrees with the SAED pattern. Figure 4C (right) shows the magnified image of the region within the red rectangle in left and the inset image is a simulated AC-HRTEM image of α -Li₅AlO₄ which viewed along zone axis [112]. The simulated image fits well with the experimental result. From the EDS mapping (Fig. 4D), La and Zr signals did not appear and there were only Al and O signals in the triangular region, which agrees with the AC-HRTEM results. As shown in Fig. 4E, under the aberration-corrected STEM mode, the electron energy-loss spectroscopy (EELS) mapping of Li element confirms the presence of lithium in the triangular grain boundary area. Apart from the α -Li₅AlO₄, the γ -LiAlO₂ second phase could also be found in the observations (Fig. 4F and Fig. S8). The second phase in the rectangular grain boundary area was identified to be γ -LiAlO₂ through SAED (Fig. 4F right), and the corresponding EDS mapping was shown in Fig. 4G.

The reactions of alumina as sintering aid are presented here: during the high-temperature sintering process, the Li element will loss in the form of evaporated Li₂O gas. Li₂O will react with alumina to form a Li-Al-O second phase with a composition as LiAlO₂ or Li₅AlO₄ over the grain boundaries as following reactions^{36,37}:



The alumina-assisted liquid phase sintering proceeds in a sequence of three stages: i) melt formation; ii) grain rearrangement; and iii) solution reprecipitation with concomitant grain growth. The “transient” liquid phase of Li-Al-O forms initially according to above reactions and preferentially penetrates pores between LLZTO particles by capillaries. The liquid phase would then create an attractive force between LLZTO particles and cause microstructural rearrangement by improving particle contact. Furthermore, effective densification can be achieved through facile mass transport by the Li-Al-O phase as well as the solution reprecipitation process, as proven by the increased grain size and reduced porosity. Finally, the Li-Al-O

phase is segregated along the grain boundaries of the LLZTO matrix. For the LLZTO+alumina sample, the second phase tends to accumulate and thus a large number of pores remain. However, for LLZTO@alumina, the homogeneous distribution of sintering additive leads to the results that pores are fully filled up by the second phase, and thus a more compact structure and a higher relative density.

Mechanical Properties

In a battery, Li-metal deposition requires extra volume around the deposition sites, which can generate large mechanical stress driven by a small over potential according to the Nernst equation. The electrochemically generated mechanical stresses may drive the formation of Griffith crack. Since the continuous Li deposition into the crack is kinetically favored, forming Li dendrites will wedge crack propagation along grain boundaries and finally short the battery³⁸⁻⁴⁰. Therefore, the mechanical strength enhancement of the entire electrolyte, especially for the grain boundaries, will be a promising way to inhibit dendrite growth. Firstly, as shown in Video S1, we applied in-situ TEM pillar compression of single crystal LLZTO. The pillar deformed mainly elastically, and yielded a Young's Modulus of ~120 GPa, which is close to the reported value (~140 GPa)⁴¹. The three-point bending test (Fig. 3J) indicates that the LLZTO@alumina pellets sintered at 1000 and 1100 °C have higher fracture strength of 57.2 and 79.1 MPa, compared with the LLZTO+alumina pellets of 28.9 and 42.2 MPa, respectively. Similar to the fracture strength, Vickers hardness of LLZTO@alumina pellets sintered at 1000 and 1100 °C have higher values of 4.72 and 5.32 GPa, respectively (Fig. S9). The improved mechanical properties of LLZTO@alumina pellets are attributed to the enhanced relative density and strengthened grain boundaries by the conformal second phases that are uniformly distributed along grain boundaries. Consequently, a more effective suppression on Li dendrite growth and enhanced electrochemical performances can be expected for the LLZTO@alumina pellets.

Electrochemical Performances

The electrochemical performances of the LLZTO ceramic electrolyte are investigated. The electrochemical impedance spectroscopy (EIS) plots of the LLZTO pellets (Fig. S10) consist of a quasi-semicircle at high frequencies corresponding to the grain and grain boundary resistances, and a long tail at low frequencies associated with the capacitive behavior of Li-ion-blocking gold electrodes. For all the LLZTO samples, the detailed sintering condition, relative density, ionic conductivity and so on, are listed in Table 1. The ionic conductivities of LLZTO w/o alumina-1100, LLZTO w/o alumina-1200, LLZTO+alumina-1000, LLZTO+alumina-1100, LLZTO@alumina-980, LLZTO@alumina-1000 and LLZTO@alumina-1100 are 0.04, 0.27, 0.09, 0.38, 0.13, 0.43 and 0.44 mS cm⁻¹ at room temperature (RT), respectively. We can find that the ionic conductivities are positively related to relative density⁴². The reduction of grain boundary impedance owing to the pores between grain boundaries could be effectively compensated by the forming of ionic conductive second phases. To date to our knowledge, the sintering temperature of 980 °C for LLZTO@alumina with RT ionic conductivity of ~0.13 mS cm⁻¹ is the lowest one among the publications about garnet electrolytes using alumina as sintering aid (Table 2).

We plotted the Debye plot (Z'' versus $\log f$) and fitted it using a Lorentzian function, which indicates the relaxation time is associated with ion hopping (Fig. 5A). The frequencies of the peak maxima, a characteristic frequency of the conductivity relaxation, can be given by the reciprocal of the conductivity relaxation time (τ) or conductivity (σ)^{43,44}:

$$2\pi f_{max} = \omega = (\tau)^{-1} = \sigma(\epsilon_0 \epsilon')^{-1} \quad (3)$$

where ϵ' (real component of permittivity) is the frequency-independent permittivity, and ϵ_0 is the permittivity of free space (8.854×10^{-14} F cm⁻¹). To be noted, the data tested at 0 °C was used for analysis as the characteristic frequency of garnet electrolyte is always quite high at room temperature. It can be seen that the characteristic frequencies of samples with higher ionic conductivity shifted toward higher frequency range, implying a faster relaxation process. It can also be seen from Fig. 5B that, Arrhenius curves showed LLZTO@alumina samples had the lowest activation energy (0.42 eV).

Recently, it has been proposed that the existence of electron conduction can lead to the formation of Li metal in SEs. The DC polarization method was applied to measure the electronic conductivity of LLZTO electrolyte pellets (Fig. S11). According to the steady current, the electronic conductivities of LLZTO w/o alumina-1200, LLZTO+alumina-1100 and LLZTO@alumina-1000 are calculated to be 8.3×10^{-9} , 8.3×10^{-9} and 4.8×10^{-9} S cm⁻¹ at 2.5 V, respectively. In addition, the electronic conductivities at different voltages were shown in Fig. 5C, we can see that the electronic conductivity of LLZTO@alumina-1000 is lower than that of LLZTO w/o alumina-1200 and LLZTO+alumina-1100 over the potential range of 1.0 V-2.5 V. The LLZTO@alumina pellet has the lowest electronic conductivity, since the Li-Al-O second phase with low electronic conductivity could modify the grain boundaries. The increase of electronic conductivity with increasing voltage is due to the growing of hole conduction⁴⁵.

Furthermore, the performances of the lithium symmetry cells based on LLZTO have also been investigated. The EIS plots of Li|LLZTO|Li with equivalent circuit are shown in Fig. S12, wherein R_{pellet} and $R_{\text{interface}}$ represented the total resistance of electrolyte pellet and the interfacial resistance, respectively. The Li|LLZTO+alumina-1100|Li and Li|LLZTO@alumina-1000|Li showed nearly overlapped curves, indicating they have the similar ionic conductivities and area specific resistance (ASR) of 35 Ω cm² for the Li|electrolyte interface. Note that because they have similar ionic conductivities, LLZTO+alumina-1100 and LLZTO@alumina-1000 were chosen for the CCD comparison. As shown in Fig. 5D, through galvanostatic cycling with step-up current densities, the CCD values of LLZTO w/o alumina, LLZTO+alumina and LLZTO@alumina were measured to be 0.08, 0.36 and 0.52 mA cm⁻², respectively, indicating the reduction of electronic conductivity can facilitate the enhancement of CCD. Besides CCD, the long-term cycling is also essential for practical SSLMBs. The cycling performances of Li|LLZTO+alumina|Li and Li|LLZTO@alumina|Li symmetrical cells were tested at the current density of 0.1 mA cm⁻² with a plating/stripping capacity of 0.1 mAh cm⁻². As shown in Fig. 5E, for the Li|LLZTO+alumina|Li cell, short-circuit occurred after only about 500 h, while the Li|LLZTO@alumina|Li cell exhibited a stable running over 5000 h without short-circuit. Nearly ten-fold improvement of cycling

life indicates that the LLZTO@alumina ceramic pellets have improved inhibition ability for Li dendrite growth after grain boundary modification.

Applying high-voltage cathode material is believed to be an effective pathway toward the goal of 500 Wh kg⁻¹⁴⁶. Since LLZTO electrolytes possess a high voltage window, a high-voltage Li_{1.2}Ni_{0.2}Mn_{0.6}O₂ (LNMO) cathode material was used to assemble a half cell based on LLZTO@alumina pellet with a tiny amount of liquid electrolyte to wet the cathode interface (Li|LLZTO@alumina|LNMO). The EIS and corresponding equivalent circuit used for fitting are shown in Fig. S13, wherein R_{pellet} is corresponding to the sum of bulk and grain boundary resistance, and R_1 and R_2 represent the area specific resistances (ASRs) of the Li|LLZTO interface and LLZTO|LNMO interface, respectively. The high-voltage battery can stably run within a voltage range of 2.0-4.8 V (vs. Li⁺/Li) at RT. Figure 5F exhibited the charge-discharge curves at 0.05 C-rate, indicating a typical electrochemical behavior of the Li-rich layered cathode material. The slope potential region below 4.5 V is attributed to the extraction of Li⁺ from the layered oxide structure, which is accompanied by Ni²⁺ oxidation, and the region above 4.5 V represents the oxygen loss from the Li₂MnO₃ component⁴⁷. The capacity and Coulombic efficiency at various C rates ranging from 0.05 to 0.5 C are shown in Fig. 5G. When cycling at 0.05 C, 0.1 C, 0.2 C, 0.3 C, 0.4 C and 0.5 C, the capacities remained 248, 233, 216, 202, 189 and 178 mAh g⁻¹, respectively. Finally, the capacity returned to 235 mAh g⁻¹ at 0.05 C, showing a good rate performance. Besides, as shown in Fig. 5H, the high-voltage cell also exhibited a good long-term cycling stability. Its capacity still remained 148 mAh g⁻¹ after 100 cycles at 0.5 C.

Mechanism Of Li Dendrite Suppression

It was reported that the formation of Li dendrites inside LLZTO ceramic electrolyte occurs only if two conditions are satisfied simultaneously: the presence of free electrons in LLZTO, and the overpotential triggering Li nucleation and growth inside LLZTO¹⁵. Most recent researches support a mechanism of dendrite penetration inside garnet SE in the following steps: (1) Li tends to nucleate preferentially at grain boundaries and voids, which is mainly attributed to the inhomogeneous distribution of current field and high electronic conduction of grain boundaries (Fig. 1A and B). The accumulation of Li causes extreme localized stress and thus the formation of cracks. (2) Continues Li deposition into the crack is kinetically favored. Such Li-filled cracks propagate through grain boundaries and/or voids, eventually short-circuiting the cell. It is an electrochemomechanical degradation process. Therefore, the electrochemomechanical properties of SE including mechanical strength, ionic conductivity, and electronic conductivity, will in turn affect battery performances. In our work, the even-distributed Li-Al-O second phases along grain boundaries as well as the improved relative density subsequently results in enhanced mechanical strength and ionic conductivity. Moreover, the nano-scale alumina coatings form even-distributed Li-Al-O second phases along grain boundaries during sintering, which is ionically conductive but electronically blocking according to density functional theory (DFT) calculations. For example, as shown in Fig. 6, one of the primary phase γ -LiAlO₂ in Li-Al-O second phase has fast Li-ion

migration channels at c-axis and exhibits a small Li-ion diffusion energy barrier of 0.245 eV (Fig. 6A and B). Besides, the calculated band structure and density of states of γ -LiAlO₂ (Fig. 6C and D) show γ -LiAlO₂ has a large band gap of 4.85 eV, revealing the nature of insulator. After modification using second phases, higher mechanical strength, increased ionic conductivity and reduced electronic conductivity can be successfully achieved. Therefore, the higher tolerance against Li dendrite penetration is owing to the synergistic effect of above improvements.

In summary, we report a conformal-nano-coating of amorphous alumina as sintering aid on the grain surface of LLZTO via ALD method rather than a conventional way of physical powder mixing. The sintering activity was greatly improved due to the Li-Al-O second phases formed at grain boundaries conformally. Hence, the dense ceramic can be prepared at a low sintering temperature below 1000 °C with high RT ionic conductivity of above 0.1 mS cm⁻¹. Moreover, higher mechanical strength and a lower electronic conductivity were achieved, which results in an enhancement of CCD value (0.52 mA cm⁻² at RT) and longer cycling life (over 5000 h). The Li-Al-O second phases at the grain boundaries, evidenced by atomic-scaled TEM imaging and spectroscopic analysis, promote Li-ion transport and strength grain boundaries. The current work provides a universal preparation method to reduce the sintering temperature and enhance electrochemical performance for inorganic solid electrolytes for ASSLMs, which could also extend to other structural and functional ceramic materials.

Declarations

Acknowledgments

This work was partially supported National Key Research and Development Program (2019YFA0210600), National Natural Science Foundation of China (21805185, 21905174) and Shanghai Rising-Star Program (20QA1406600). We also acknowledge CEM, SPST of ShanghaiTech University (#EM02161943) and HPC Platform of ShanghaiTech University for supporting.

Author contributions

S.C. and X.H. carried out the experiments, characterizations, data analysis, and manuscript preparation. W.B. conducted ALD. Z.W. and X.Z. conducted the DFT calculations. Q.Y. conducted the in-situ LLZO pillar compression experiments. L.N. and J.Z. helped to prepare samples. Y.J. conducted the AES measurement and analysed the results. Y.H. and C.W. conducted the test of Vickers hardness and analysed the results. J.X. helped to review the results. Y.Y. and W.L. managed the project and reviewed the results, data analysis and manuscript preparation.

Competing interests

The authors declare no competing interests.

References

- 1 Dunn, B., Kamath, H. & Tarascon, J. M. Electrical energy storage for the grid: A battery of choices. *Science* **334**, 928-935 (2011).
- 2 Li, M., Lu, J., Chen, Z. & Amine, K. 30 years of lithium-ion batteries. *Adv. Mater.*, e1800561 (2018).
- 3 Chen, T. et al. Applications of lithium-ion batteries in grid-scale energy storage systems. *Transactions of Tianjin University* **26**, 208-217 (2020).
- 4 Thangadurai, V., Narayanan, S. & Pinzaru, D. Garnet-type solid-state fast Li ion conductors for Li batteries: Critical review. *Chem. Soc. Rev.* **43**, 4714-4727 (2014).
- 5 Goodenough, J. B. How we made the li-ion rechargeable battery. *Nature Electronics* **1**, 204-204 (2018).
- 6 Manthiram, A., Yu, X. & Wang, S. Lithium battery chemistries enabled by solid-state electrolytes. *Nature Reviews Materials* **2** (2017).
- 7 Tan, D. H. S., Banerjee, A., Chen, Z. & Meng, Y. S. From nanoscale interface characterization to sustainable energy storage using all-solid-state batteries. *Nat. Nanotechnol.* **15**, 170-180 (2020).
- 8 Chen, S. et al. All-solid-state batteries with a limited lithium metal anode at room temperature using a garnet-based electrolyte. *Adv. Mater.*, e2002325 (2020).
- 9 Bachman, J. C. et al. Inorganic solid-state electrolytes for lithium batteries: Mechanisms and properties governing ion conduction. *Chem. Rev.* **116**, 140-162 (2016).
- 10 Dai, J., Yang, C., Wang, C., Pastel, G. & Hu, L. Interface engineering for garnet-based solid-state lithium-metal batteries: Materials, structures, and characterization. *Adv. Mater.* **30**, e1802068 (2018).
- 11 Gao, Z. et al. Promises, challenges, and recent progress of inorganic solid-state electrolytes for all-solid-state lithium batteries. *Adv. Mater.* **30**, e1705702 (2018).
- 12 Chen, R., Li, Q., Yu, X., Chen, L. & Li, H. Approaching practically accessible solid-state batteries: Stability issues related to solid electrolytes and interfaces. *Chem. Rev.* (2019).
- 13 Song, Y. et al. Revealing the short-circuiting mechanism of garnet-based solid-state electrolyte. *Advanced Energy Materials* **9** (2019).
- 14 Monroe, C. & Newman, J. The impact of elastic deformation on deposition kinetics at lithium/polymer interfaces. *J. Electrochem. Soc.* **152** (2005).
- 15 Han, F. et al. High electronic conductivity as the origin of lithium dendrite formation within solid electrolytes. *Nat. Energy* **4**, 187-196 (2019).
- 16 Krauskopf, T. et al. Lithium-metal growth kinetics on llzo garnet-type solid electrolytes. *Joule* **3**, 2030-2049 (2019).

- 17 Porz, L. et al. Mechanism of lithium metal penetration through inorganic solid electrolytes. *Advanced Energy Materials* **7** (2017).
- 18 Ren, Y., Shen, Y., Lin, Y. & Nan, C.-W. Direct observation of lithium dendrites inside garnet-type lithium-ion solid electrolyte. *Electrochem. Commun.* **57**, 27-30 (2015).
- 19 Cheng, E. J., Sharafi, A. & Sakamoto, J. Intergranular Li metal propagation through polycrystalline $\text{Li}_{6.25}\text{Al}_{0.25}\text{La}_3\text{Zr}_2\text{O}_{12}$ ceramic electrolyte. *Electrochim. Acta* **223**, 85-91 (2017).
- 20 Yue, J. & Guo, Y.-G. The devil is in the electrons. *Nat. Energy* **4**, 174-175 (2019).
- 21 Tian, H.-K., Liu, Z., Ji, Y., Chen, L.-Q. & Qi, Y. Interfacial electronic properties dictate Li dendrite growth in solid electrolytes. *Chem. Mater.* **31**, 7351-7359 (2019).
- 22 Tian, H.-K., Xu, B. & Qi, Y. Computational study of lithium nucleation tendency in $\text{Li}_7\text{La}_3\text{Zr}_2\text{O}_{12}$ (LLZO) and rational design of interlayer materials to prevent lithium dendrites. *J. Power Sources* **392**, 79-86 (2018).
- 23 Randau, S. et al. Benchmarking the performance of all-solid-state lithium batteries. *Nat. Energy* **5**, 259-270 (2020).
- 24 Pfenninger, R., Struzik, M., Garbayo, I., Stilp, E. & Rupp, J. L. M. A low ride on processing temperature for fast lithium conduction in garnet solid-state battery films. *Nat. Energy* **4**, 475-483 (2019).
- 25 Park, K. et al. Electrochemical nature of the cathode interface for a solid-state lithium-ion battery: Interface between LiCoO_2 and garnet- $\text{Li}_7\text{La}_3\text{Zr}_2\text{O}_{12}$. *Chem. Mater.* **28**, 8051-8059 (2016).
- 26 Liu, T. et al. Enhanced electrochemical performance of bulk type oxide ceramic lithium batteries enabled by interface modification. *Journal of Materials Chemistry A* **6**, 4649-4657 (2018).
- 27 El-Shinawi, H., Cussen, E. J. & Corr, S. A. Enhancement of the lithium ion conductivity of Ta-doped $\text{Li}_7\text{La}_3\text{Zr}_2\text{O}_{12}$ by incorporation of calcium. *Dalton Trans* **46**, 9415-9419 (2017).
- 28 Fang, Y., Liu, X., Feng, Y., Zhu, J. & Jiang, W. Microstructure and mechanical properties of $\text{Ti}_3(\text{Al,Ga})\text{C}_2/\text{Al}_2\text{O}_3$ composites prepared by in situ reactive hot pressing. *Journal of Advanced Ceramics* (2020).
- 29 Aboulaich, A. et al. A new approach to develop safe all-inorganic monolithic Li-ion batteries. *Advanced Energy Materials* **1**, 179-183 (2011).
- 30 Zhong, G. et al. Rapid, high-temperature microwave soldering toward a high-performance cathode/electrolyte interface. *Energy Storage Materials* **30**, 385-391 (2020).

- 31 Wang, Y. et al. Effect of Al_2O_3 on the sintering of garnet-type $\text{Li}_{6.5}\text{La}_3\text{Zr}_{1.5}\text{Ta}_{0.5}\text{O}_{12}$. *Solid State Ionics* **294**, 108-115 (2016).
- 32 Kotobuki, M., Kanamura, K., Sato, Y. & Yoshida, T. Fabrication of all-solid-state lithium battery with lithium metal anode using Al_2O_3 -added $\text{Li}_7\text{La}_3\text{Zr}_2\text{O}_{12}$ solid electrolyte. *J. Power Sources* **196**, 7750-7754 (2011).
- 33 Deng, F. et al. Conformal, nanoscale $\gamma\text{-Al}_2\text{O}_3$ coating of garnet conductors for solid-state lithium batteries. *Solid State Ionics* **342** (2019).
- 34 Janani, N., Deviannapoorani, C., Dhivya, L. & Murugan, R. Influence of sintering additives on densification and Li^+ conductivity of Al doped $\text{Li}_7\text{La}_3\text{Zr}_2\text{O}_{12}$ lithium garnet. *RSC Adv.* **4**, 51228-51238 (2014).
- 35 Huang, X. et al. None-mother-powder method to prepare dense Li-garnet solid electrolytes with high critical current density. *ACS Applied Energy Materials* (2018).
- 36 Huang, X. et al. Manipulating Li_2O atmosphere for sintering dense $\text{Li}_7\text{La}_3\text{Zr}_2\text{O}_{12}$ solid electrolyte. *Energy Storage Materials* **22**, 207-217 (2019).
- 37 Ren, Y. et al. Effects of Li source on microstructure and ionic conductivity of Al-contained $\text{Li}_{6.75}\text{La}_3\text{Zr}_{1.75}\text{Ta}_{0.25}\text{O}_{12}$ ceramics. *J. Eur. Ceram. Soc.* **35**, 561-572 (2015).
- 38 Wang, Z. et al. Creep-enabled 3d solid-state lithium-metal battery. *Chem* (2020).
- 39 Chen, Y. et al. Li metal deposition and stripping in a solid-state battery via coble creep. *Nature* **578**, 251-255 (2020).
- 40 Famprakis, T., Canepa, P., Dawson, J. A., Islam, M. S. & Masquelier, C. Fundamentals of inorganic solid-state electrolytes for batteries. *Nat Mater* **18**, 1278-1291 (2019).
- 41 Wang, A.-N. et al. Mechanical properties of the solid electrolyte Al-substituted $\text{Li}_7\text{La}_3\text{Zr}_2\text{O}_{12}$ (LLZO) by utilizing micro-pillar indentation splitting test. *J. Eur. Ceram. Soc.* **38**, 3201-3209 (2018).
- 42 Krauskopf, T., Hartmann, H., Zeier, W. G. & Janek, J. Toward a fundamental understanding of the lithium metal anode in solid-state batteries-an electrochemo-mechanical study on the garnet-type solid electrolyte $\text{Li}_{6.25}\text{Al}_{0.25}\text{La}_3\text{Zr}_2\text{O}_{12}$. *ACS Appl Mater Interfaces* **11**, 14463-14477 (2019).
- 43 Liu, W. et al. Enhancing ionic conductivity in composite polymer electrolytes with well-aligned ceramic nanowires. *Nat. Energy* **2** (2017).
- 44 Dash, U., Sahoo, S., Parashar, S. K. S. & Chaudhuri, P. Effect of Li^+ ion mobility on the grain boundary conductivity of Li_2TiO_3 nanoceramics. *Journal of Advanced Ceramics* **3**, 98-108 (2014).

- 45 Buschmann, H. et al. Structure and dynamics of the fast lithium ion conductor " $\text{Li}_7\text{La}_3\text{Zr}_2\text{O}_{12}$ ". *Phys. Chem. Chem. Phys.* **13**, 19378-19392 (2011).
- 46 Liu, J. et al. Pathways for practical high-energy long-cycling lithium metal batteries. *Nat. Energy* **4**, 180-186 (2019).
- 47 Nie, L. et al. Biofilm nanofiber-coated separators for dendrite-free lithium metal anode and ultrahigh-rate lithium batteries. *ACS Appl Mater Interfaces* **11**, 32373-32380 (2019).
- 48 Huang, X. et al. A li-garnet composite ceramic electrolyte and its solid-state Li-S battery. *J. Power Sources* **382**, 190-197 (2018).
- 49 Xia, W. et al. Ionic conductivity and air stability of al-doped $\text{Li}_7\text{La}_3\text{Zr}_2\text{O}_{12}$ sintered in alumina and pt crucibles. *ACS Appl Mater Interfaces* **8**, 5335-5342 (2016).
- 50 Alexander, G. V. et al. Electrodes-electrolyte interfacial engineering for realizing room temperature lithium metal battery based on garnet structured solid fast Li^+ conductors. *J. Power Sources* **396**, 764-773 (2018).
- 51 Li, Y., Han, J.-T., Wang, C.-A., Xie, H. & Goodenough, J. B. Optimizing Li^+ conductivity in a garnet framework. *J. Mater. Chem.* **22** (2012).
- 52 He, M., Cui, Z., Chen, C., Li, Y. & Guo, X. Formation of self-limited, stable and conductive interfaces between garnet electrolytes and lithium anodes for reversible lithium cycling in solid-state batteries. *Journal of Materials Chemistry A* **6**, 11463-11470 (2018).
- 53 El-Shinawi, H., Paterson, G. W., MacLaren, D. A., Cussen, E. J. & Corr, S. A. Low-temperature densification of Al-doped $\text{Li}_7\text{La}_3\text{Zr}_2\text{O}_{12}$: A reliable and controllable synthesis of fast-ion conducting garnets. *Journal of Materials Chemistry A* **5**, 319-329 (2017).

Tables

Table 1

Performances of LLZTO solid electrolytes at different sintering conditions.

Samples	Sintering temp (°C)	Relative density	σ_t (mS cm ⁻¹)	σ_b (mS cm ⁻¹)	σ_{gb} (mS cm ⁻¹)	C _{gb} (F)	Active energy (eV)
LLZTO w/o alumina	1100	86.5%	0.04	0.80	0.04	3.70E-11	0.54±0.01
LLZTO w/o alumina	1200	91.0%	0.27	2.12	0.31	6.38E-11	0.44±0.01
LLZTO+alumina	980	78.8%	0.03	1.09	0.03	3.74E-11	0.56±0.01
LLZTO+alumina	1000	86.3%	0.09	1.06	0.10	6.31E-11	0.50±0.01
LLZTO+alumina	1100	90.9%	0.38	2.11	0.47	5.41E-11	0.43±0.01
LLZTO@alumina	980	87.8%	0.13	2.08	0.14	6.74E-11	0.49±0.01
LLZTO@alumina	1000	93.2%	0.43	2.10	0.53	9.01E-11	0.42±0.01
LLZTO@alumina	1100	93.5%	0.44	2.17	0.55	8.71E-11	0.42±0.01

Table 2

Sintering temperature and performance comparison of the LLZTO electrolyte with that of previously reported garnet-type electrolytes.

Composition	Method	Sintering additive	Sintering condition	Ionic conductivity (mS cm ⁻¹)	Temp.	Ref.
Li _{6.4} La ₃ Zr _{1.4} Ta _{0.6} O ₁₂	SSR	N/A	1250 °C/10 h	0.67	RT	48
Li _{6.4} La ₃ Zr _{1.4} Ta _{0.6} O ₁₂	SSR	N/A	1250 °C/0.67 h	0.65	25 °C	35
Li ₇ La ₃ Zr ₂ O ₁₂	SSR	N/A	1200 °C/24 h	0.18	RT	49
Li _{6.28} Al _{0.24} La ₃ Zr ₂ O ₁₂	SSR	N/A	1200 °C/20 h	0.35	25 °C	50
Li _{6.5} La ₃ Zr _{1.5} Ta _{0.5} O ₁₂	SSR	N/A	1140 °C/16 h	1.00	RT	51
Li _{6.375} La ₃ Zr _{1.375} Nb _{0.625} O ₁₂	SSR*	N/A	1150 °C/1 h	1.37	RT	52
Li _{6.3} La _{2.9} Ca _{0.2} Zr _{1.4} Ta _{0.6} O ₁₂	Sol-gel*	N/A	1000 °C/0.33 h	0.20	RT	27
Li _{6.25} Al _{0.25} La ₃ Zr ₂ O ₁₂	PLD	Li ₃ N	660 °C/0.25 h	0.03	23 °C	24
Li _{6.75} La ₃ Zr _{1.75} Ta _{0.25} O ₁₂	SSR	alumina	1150 °C/12 h	0.44	RT	33
Li _{6.75} La ₃ Zr _{1.75} Ta _{0.25} O ₁₂	SSR	alumina	1200 °C/4 h	0.61	RT	37
Li _{6.5} La ₃ Zr _{1.5} Ta _{0.5} O ₁₂	SSR	alumina	1100 °C/12 h	0.49	RT	31
Li ₇ La ₃ Zr ₂ O ₁₂	SSR	alumina	1100 °C/3 h	0.30	25 °C	53
Li ₇ La ₃ Zr ₂ O ₁₂	SSR	alumina	1000 °C/36 h	0.14	30 °C	32
Li _{6.4} La ₃ Zr _{1.4} Ta _{0.6} O ₁₂	SSR	alumina	1000 °C/12 h	0.43	25 °C	This work
Li _{6.4} La ₃ Zr _{1.4} Ta _{0.6} O ₁₂	SSR	alumina	980 °C/12 h	0.13	25 °C	This work

Note: *represent the solid electrolyte was prepared by hot-press.

Figures

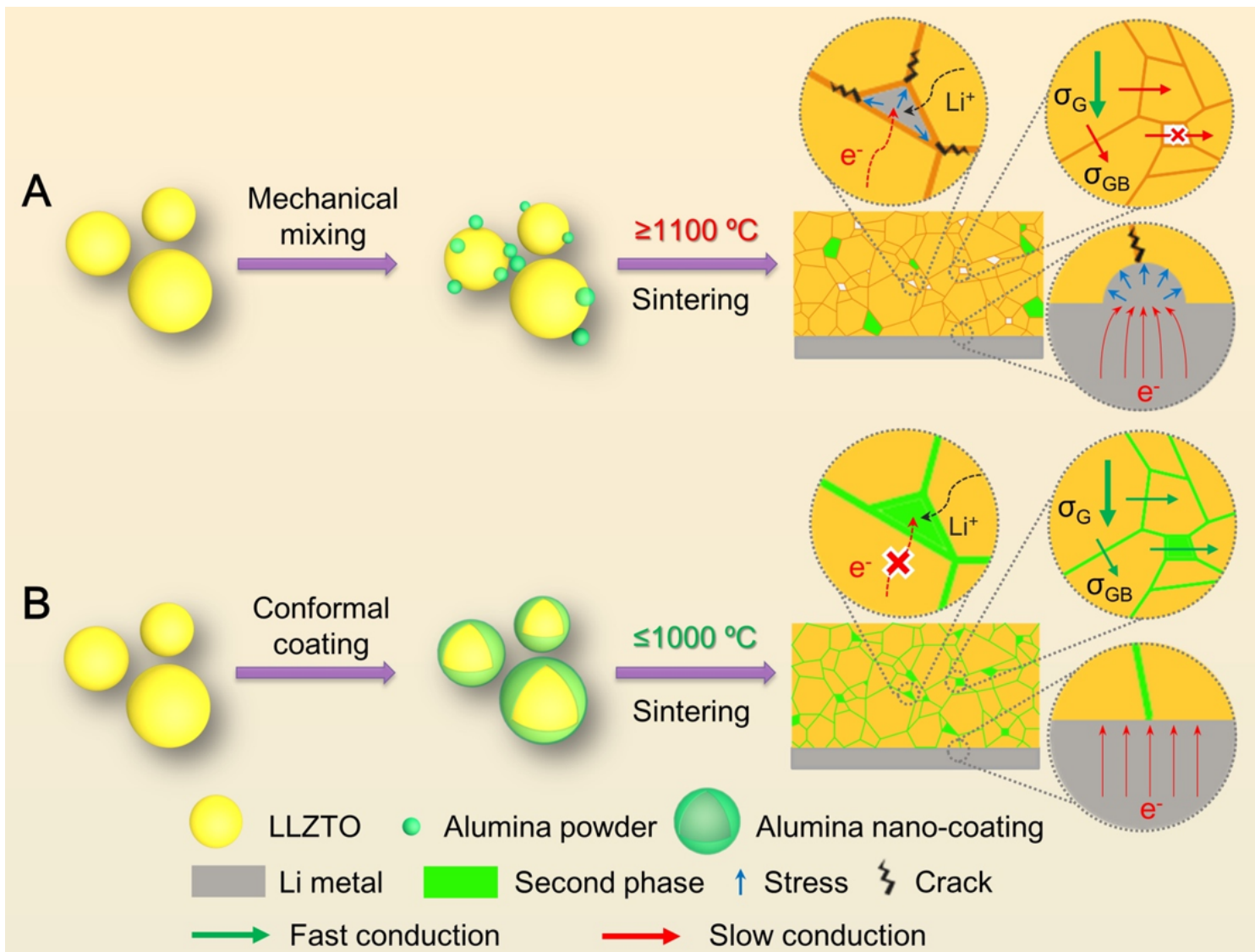


Figure 1

Schematic diagram of different microstructures of garnet-type solid electrolyte prepared by conventional pressureless sintering with sintering aid by traditional ball milling and conformal nano-coating. (A) Garnet oxide ceramic prepared by traditional method of physically mixing alumina powders as sintering aid requires sintering temperatures higher than $1100\text{ }^{\circ}\text{C}$. For the garnet ceramic sintered below $1100\text{ }^{\circ}\text{C}$ shows low relative density with low conductive grain boundary and pores where Li dendrite preferred to grow. (B) Garnet oxide with conformal nano-coating of alumina layer as sintering aid via ALD can guarantee low sintering temperatures below $1000\text{ }^{\circ}\text{C}$. The garnet ceramic with high relative density shows second phases with high conductivity and low electronic conductivity are evenly distributed at grain boundaries, which contribute to suppressing the forming of Li dendrites .

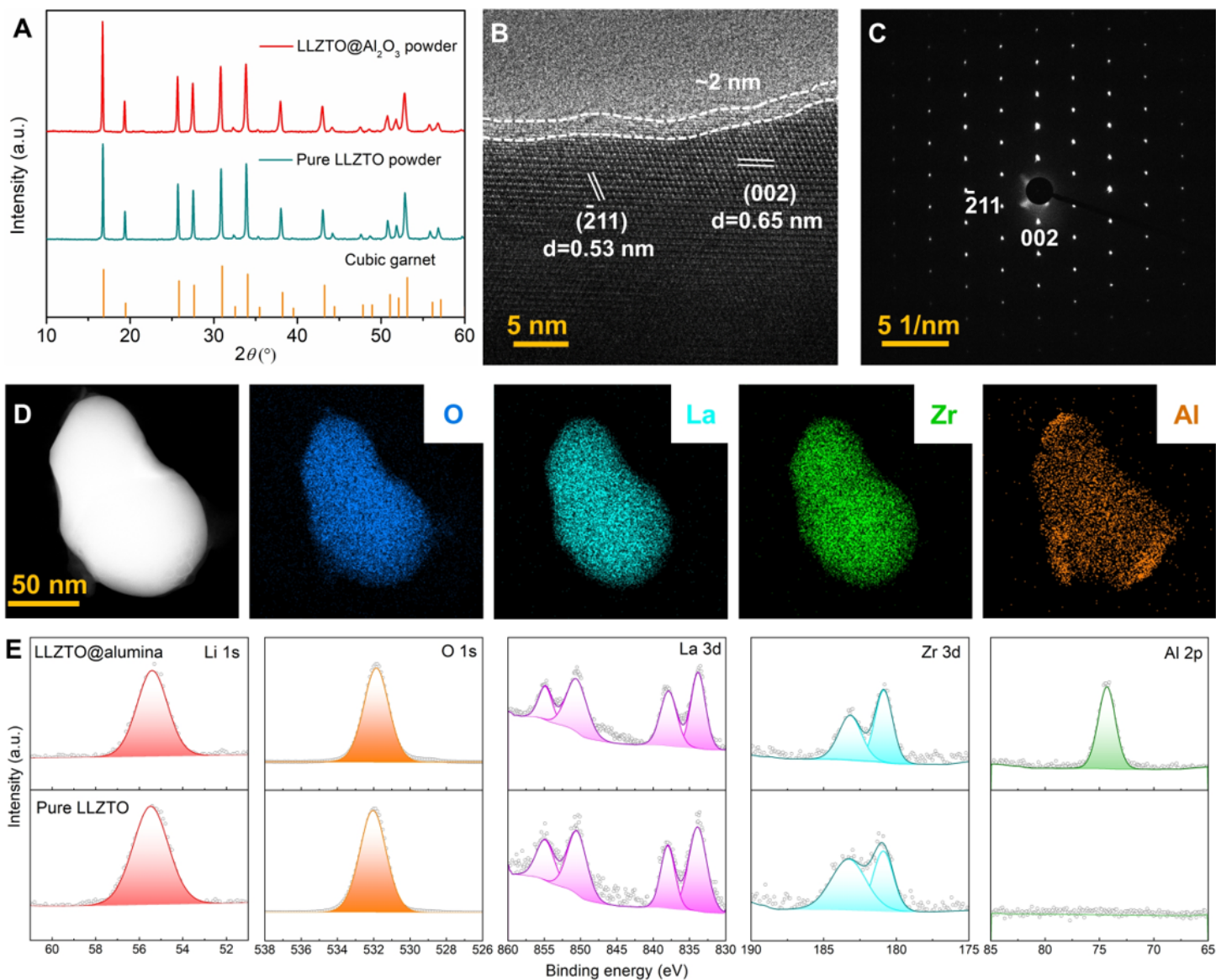


Figure 2

Structure characterization of LLZTO@alumina particles. (A) XRD patterns of pure LLZTO and LLZTO@alumina powders. (B) HRTEM image of LLZTO@alumina particle. (C) According SAED image which viewed along zone axis [120]. (D) EDS mapping images of LLZTO@alumina particle. (E) XPS data of pure LLZTO and LLZTO@alumina powders, respectively.

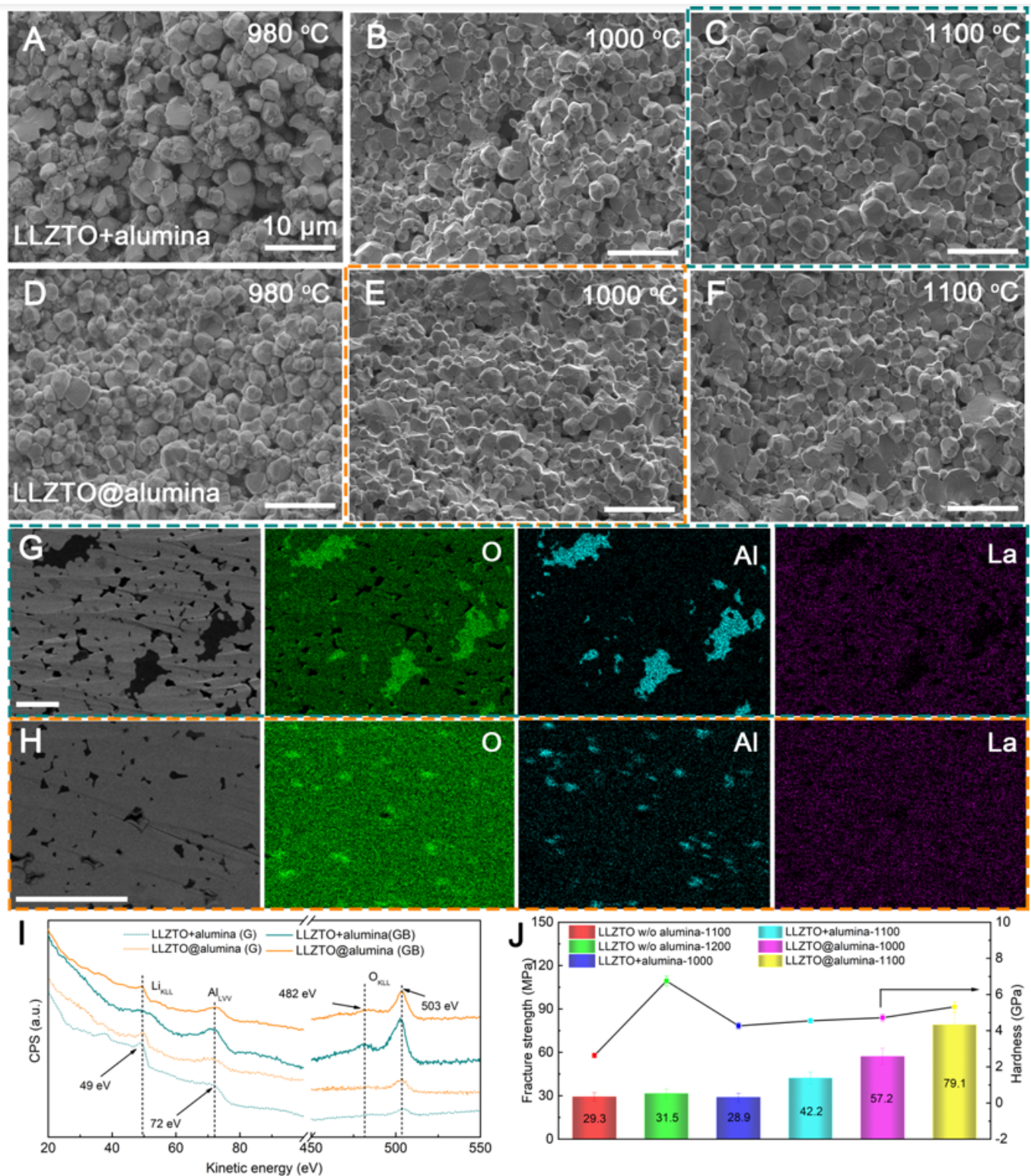


Figure 3

Microstructures and mechanical properties of different garnet pellets sintered at different conditions. (A to C) Cross section SEM images of LLZTO+alumina pellets sintered at 980, 1000 and 1100 °C. (D to F) Cross section SEM images of LLZTO@alumina pellets sintered at 980, 1000 and 1100 °C. (G and H) EDS mappings of LLZTO+alumina-1100 and LLZTO@alumina-1000, respectively. Scale bar is 10 μm . (I) AES

spectra of grain and grain boundary of the LLZTO+alumina and LLZTO@alumina pellets. (J) The fracture strength and hardness of different LLZTO pellets.

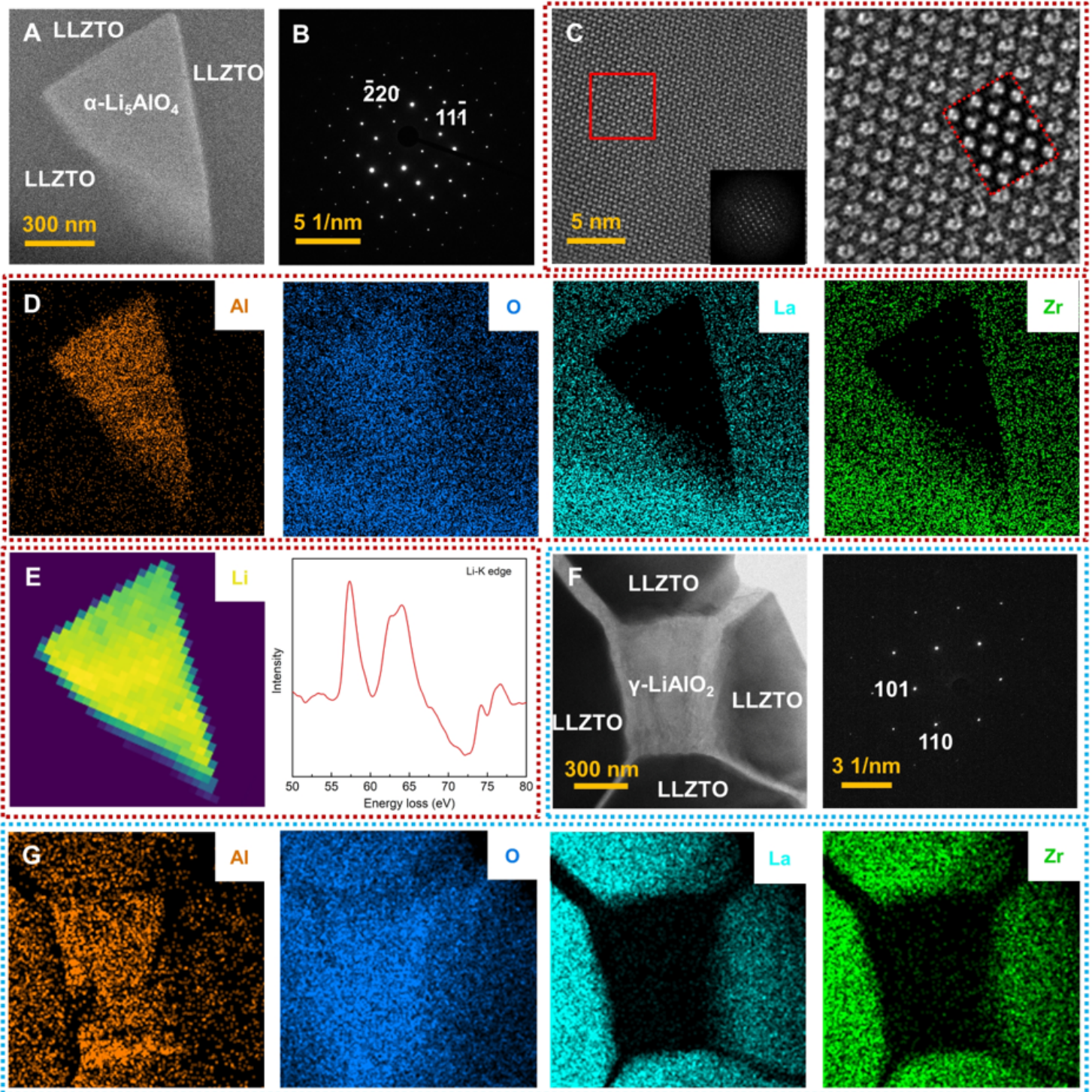


Figure 4

Aberration-corrected TEM characterization of LLZTO@alumina pellet. (A) TEM image of the triangular grain boundary region. (B) SAED pattern taken from triangular area in (A). (C) Left: aberration-corrected high-resolution TEM (AC-HRTEM) image of second phase. Right: magnified image of the region within the red rectangle in left and the inset image is simulated HRTEM image of $\alpha\text{-Li}_5\text{AlO}_4$ which viewed along

zone axis [112]. (D) EDS mapping of the triangular grain boundary region. (E) The corresponding EELS mapping of Li element. (F) Left: TEM image of the rectangular grain boundary region. Right: SAED pattern taken from rectangular area which viewed along zone axis $[\bar{1}11]$. (G) Corresponding EDS mapping images.

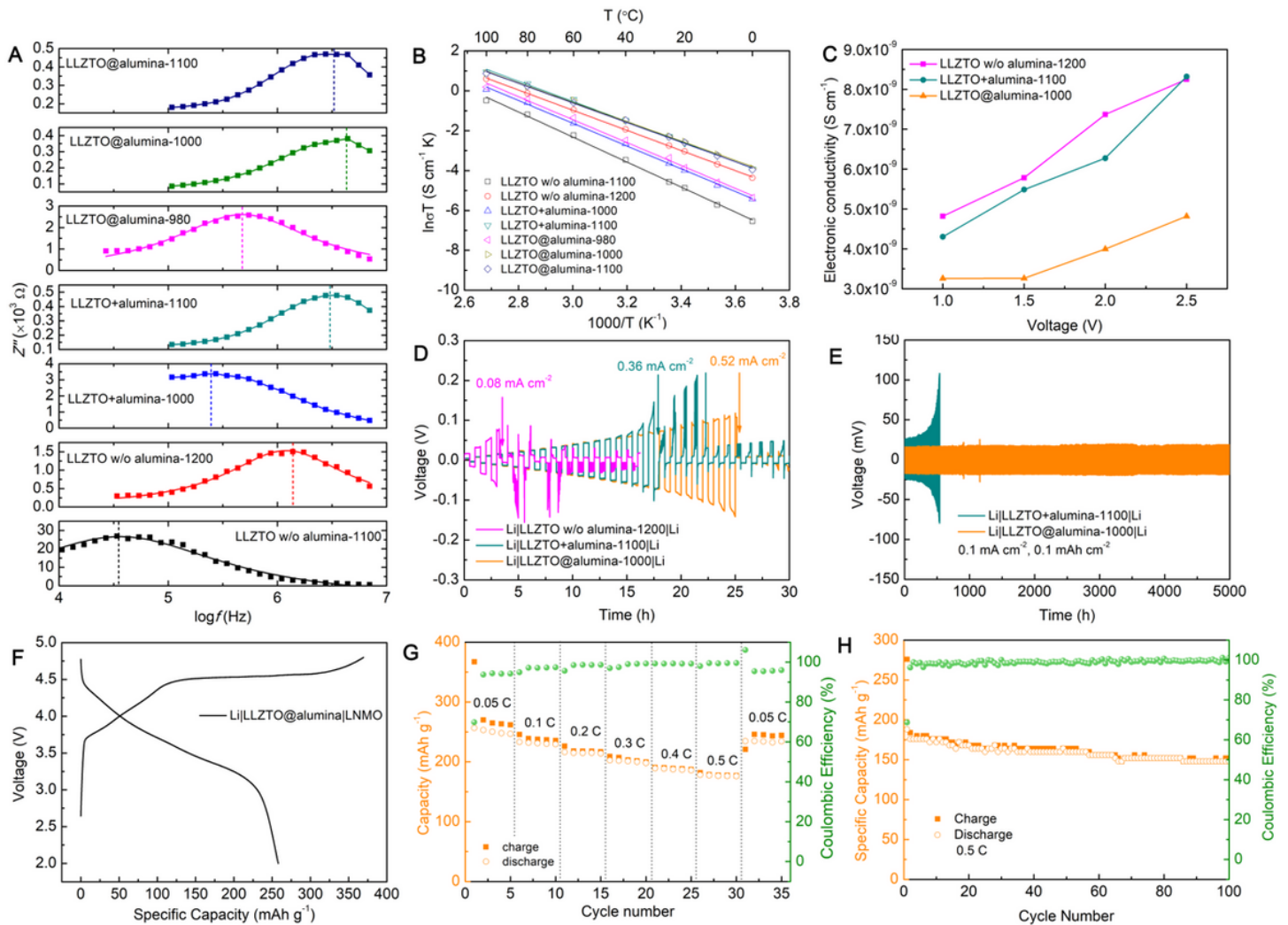


Figure 5

Characterization of electrochemical performance. (A) Representative plots of imaginary impedance as a function of the $\log f$ (Nyquist plots) and fitting curves for the different LLZTO electrolytes, measured at 0 °C. The vertical lines indicate the Debye peak positions. (B) Arrhenius plots of different LLZTO pellets. (C) Electronic conductivity of various LLZTO pellets with different applied external voltages. (D) Lithium plating-stripping performance of various Li symmetry cells at different current densities. (E) Cycling performance of Li|LLZTO+alumina-1100|Li and Li|LLZTO@alumina-1000|Li symmetry cells. (F) Charge-discharge curves of the Li|LLZTO@alumina|LNMO cells under 0.05 C-rate. (G) Rate capability of the cells at various C rates from 0.05 C to 0.5 C. (H) Cycling performance and corresponding Coulombic efficiency of Li|LLZTO@alumina|LNMO cells.

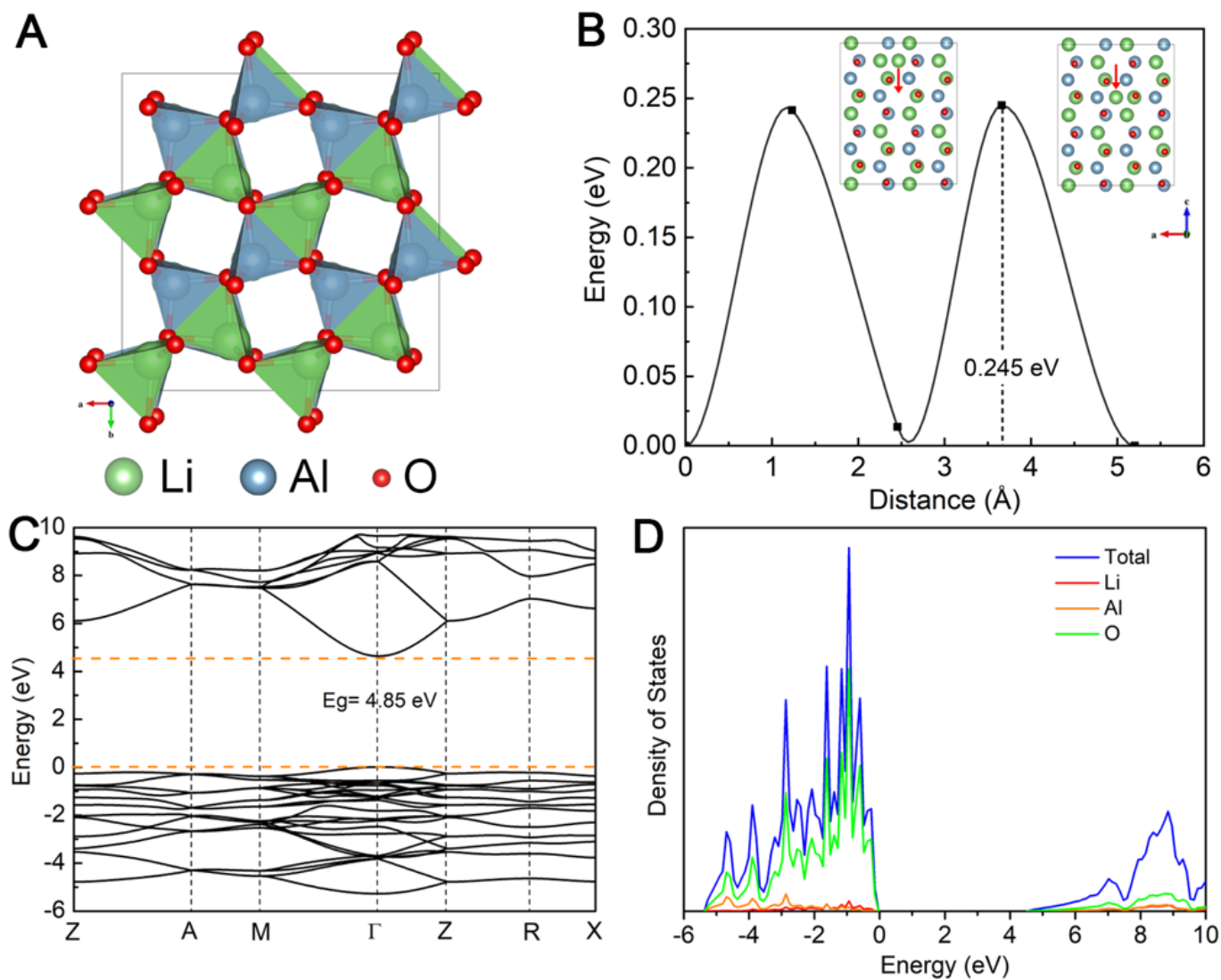


Figure 6

DFT calculations about γ -LiAlO₂. (A) The crystal structure of γ -LiAlO₂. (B) Energy profile diagram for the Li-ion diffusion. The calculated electronic properties of γ -LiAlO₂: band structure (C) and density of states (D).

Supplementary Files

This is a list of supplementary files associated with this preprint. Click to download.

- [SupplementaryInformation.docx](#)
- [VideoS1.mp4](#)